

Simple shear deformation of olivine aggregates

Shuqing Zhang^{a,*}, Shun-ichiro Karato^b, John Fitz Gerald^a,
Ulrich H. Faul^a, Yi Zhou^b

^a *Research School of Earth Sciences, The Australian National University, GPO Box 4, Canberra, ACT 0200, Australia*

^b *Department of Geology and Geophysics, University of Minnesota, Minneapolis, MN, USA*

Received 30 July 1999; accepted for publication 25 August 1999

Abstract

Simple shear deformation of synthetic olivine aggregates to high strains shows that dynamic recrystallisation has strong effects on the mechanical behaviour and the development of lattice preferred orientations. At 1473 K, a pronounced strain hardening is observed associated with grain elongation and limited dynamic recrystallisation along grain boundaries. The lattice preferred orientations of relict olivine grains generally follow the strain ellipsoid up to a shear strain of 1.1. Both [100] and [001] axes have peaks parallel to the maximum grain elongation direction. At 1573 K and shear strains >0.6, a moderate strain softening was associated with the development of significant dynamic recrystallisation. The lattice preferred orientation of relict olivine grains is characterised by point maxima with [100] axes parallel to the shear direction, [010] axes perpendicular to the shear plane, and [001] axes within the shear plane and perpendicular to the shear direction. The results suggest that at 1473 K both the $b=[100]$ dislocations and $b=[001]$ dislocations contribute to plastic deformation; at 1573 K dynamic recrystallisation relaxed constraints on deformation at grain boundaries, leading to a situation where a single slip system with $b=[100]$ dislocations controls the rheology and the fabric.

The lattice orientations of dynamically recrystallised olivine grains were measured using the electron backscatter diffraction technique. The measurements reveal a bimodal pattern of [100] axes: one parallel to the shear direction and the other perpendicular to the maximum principal compressive stress. Analysis of the results shows that the development of the stress-controlled orientations is closely associated with grain boundary migration processes during recrystallisation and growth. As a consequence, the direction of the fastest seismic velocity would not be parallel to the shear direction for olivine aggregates when grain boundary migration has a strong influence on the fabric. © 2000 Elsevier Science B.V. All rights reserved.

Keywords: crystallographic orientation; deformation; olivine; seismic anisotropy

1. Introduction

Microstructural development and resultant rheological behaviour of a polycrystalline rock are sensitive to deformation geometry and deforma-

tion mechanisms. In many tectonic settings, deformation geometry involves a rotational component (Nicolas, 1976, 1986; Boudier and Nicolas, 1995; Ji et al., 1996). However, most previous experimental studies on the lattice preferred orientations (LPOs) of upper mantle minerals were conducted under uniaxial compression (Avé Lallemant and Carter, 1970; Nicolas et al., 1973). Also, the maximum strains in these studies could only go to

* Corresponding author. Tel.: +61 2 6249 5167;
Fax: +61 2 6279 8253.

E-mail address: shuqing.zhang@anu.edu.au (S. Zhang)

about 50% owing to the limitations of deformation geometry, whereas in the mantle of the Earth shear strains $\gamma \geq 1-3$ are very common, as found in natural peridotites (Nicolas, 1976; Nicolas et al., 1971; Peselnick et al., 1974). Because of these differences in deformation styles between laboratory studies and the upper mantle, results of conventional laboratory studies are not easily applied to such problems as the development of an LPO and resultant seismic anisotropy, and the nature of plastic anisotropy (strain hardening or softening).

The seismic anisotropy of the upper mantle is mainly due to the plastic-deformation-induced LPO of olivine and pyroxene (Hess, 1964; Peselnick et al., 1974; Fuchs, 1977; Christensen, 1984; Karato, 1987; Nicolas and Christensen, 1987; Mainprice and Silver 1993). Seismic anisotropy, therefore, provides a potentially powerful tool to study the deformation mechanisms and flow patterns in the Earth's mantle (Babuska et al., 1993; Karato and Wu, 1993; Ji et al., 1994). To achieve this goal, it is critical to understand the relationship between the deformation geometry and the patterns of LPO. Currently, there are three different theories about the development of LPO in olivine and pyroxene: (1) flow geometry control (Nicolas et al., 1971; Etchecopar and Vasseur, 1987); (2) strain control (Takeshita and Wenk, 1990; Ribe and Yu, 1991; Wenk and Christie, 1991; Wenk et al., 1991); (3) stress control (Avé Lallemant and Carter, 1970; Carter et al., 1972; Karato, 1987). The distinction between these models is important for the interpretation of seismic anisotropy, as the fast velocity direction could represent shear direction, strain ellipsoid, or the σ_3 direction for the above three models respectively (Blackman et al., 1993; Chastel et al., 1993; Gao et al., 1994; Ji et al., 1996; Levin and Park, 1998). A clear distinction between the three models can be made through simple shear deformation experiments, but not from uniaxial (or triaxial) compression tests.

We have successfully deformed synthetic olivine aggregates in simple shear at a confining pressure of 300 MPa and temperatures of 1473 K and 1573 K. Shear strains up to 1.5 were achieved. In an earlier paper (Zhang and Karato, 1995) we

examined the effect of plastic flow by dislocation glide on the development of LPOs in large relict olivine grains. We showed that, at large strains, the microscopic slip direction [100] and slip plane (010) are aligned parallel to the macroscopic shear direction and shear plane respectively. Therefore, the experimental result supports the interpretation that flow geometry controls the development of LPOs in olivine aggregates when dislocation glide is the dominant deformation mechanism.

However, in this early work, orientations of small grains were not measured because of technical limitations. These small grains are presumably recrystallised grains that may have orientations distinct from large relict grains. Dynamic recrystallisation is commonly observed in mantle xenoliths (Mercier and Nicolas, 1975; Nicolas, 1976, 1986; Mercier, 1985) and in experimentally deformed olivine aggregates when strain exceeds a few to a few tens percent, depending on water content (Avé Lallemant and Carter, 1970; Chopra and Paterson, 1984; Zeuch and Green, 1984). In theory, the lattice orientations for dynamically recrystallised grains depend on the balance between nucleation and grain boundary mobility (Karato, 1987; Wenk et al., 1997). Thus, different recrystallisation mechanisms (subgrain rotation versus grain boundary migration) may result in very different patterns of LPOs (Karato, 1987, 1988; Lloyd and Freeman, 1994). Karato (1988) and Toriumi and Karato (1985) found that recrystallised olivine grains formed via a subgrain rotation mechanism have a similar LPO to their parent grains. These new grains should also assume the flow-geometry-controlled orientations. Kunze and Avé Lallemant (1981) conducted uniaxial compressional tests on dunite at high temperatures of 1173–1523 K and introduced a non-coaxial component of deformation in the specimens near loading pistons. Measurements of LPOs for the recrystallised grains in those regions using a universal stage and an X-ray pole-figure device showed that [010] axes are consistently aligned at angles of 30–45° to the inferred flow plane, indicating that the fabric does not reflect the shear geometry or strain ellipsoid, but possibly the stress ellipsoid.

In the sheared olivine samples that we reported earlier (Zhang and Karato, 1995), 10–50 vol.%

new grains are present. Measurement of orientations for the small ($<10\ \mu\text{m}$) new grains was not possible using the universal stage technique. Taking advantage of the electron backscatter diffraction (EBSD) technique at the Australian National University (Faul and Fitz Gerald, 1999), we have recently determined the orientations of olivine grains as small as $2\text{--}3\ \mu\text{m}$.

The objectives of the present paper are to examine (1) how the deformation mechanism, in particular the dynamic recrystallisation, influenced the rheological behaviour, and (2) what controls the lattice orientations of dynamically recrystallised grains. We will show the development of LPOs and the corresponding mechanical behaviour as a function of strain at both 1473 and 1573 K. The experimental data will provide a firm constraint for modelling the development of LPOs in polycrystalline olivine (Karato, 1987; Jessel, 1988; Wenk et al., 1997). We will firstly introduce the techniques for shear deformation and microstructural characterisation. We will then present mechanical and fabric data and finally discuss their implications.

2. Starting material and experimental techniques

2.1. Starting material

Dense olivine aggregates were obtained by hot pressing of an olivine powder finely ground from hand-picked San Carlos olivine single crystals using an agate mortar. The olivine powder was separated within water into different grain size fractions using the sedimentation method and was dried in an oven at a temperature of 423 K for about 24 h. For each hot pressing, a few grams of olivine powder was first put into a nickel can and cold-pressed in a die with a uniaxial stress of about 200 MPa. Hot isostatic pressing was conducted in an argon-gas-medium apparatus at a confining pressure of 300 MPa and a temperature of 1573 K for 4 h. After a number of trials, we found that in order to achieve a uniform grain size distribution within the hot-pressed specimen the starting powder needs to have a rather wide particle size distribution (see Fig. 1c, Karato, 1989). Practically, we mixed

50 wt% particles of $<5\ \mu\text{m}$ with 50 wt% particles of $5\text{--}10\ \mu\text{m}$. Before hot pressing, we usually put a thick disc (about 3 mm) of talc beneath the cold-pressed sample and separate them with a thin layer of nickel foil. Dehydration of talc at high temperature releases water and enhances the grain growth of olivine (Karato, 1989).

The typical microstructure of hot-pressed olivine is shown in Fig. 1a. The average grain size is about $35\ \mu\text{m}$ (Table 1). Small ($1\text{--}2\ \mu\text{m}$) bubbles are present inside many grains (Fig. 1a) and they are most likely the entrapped free water during grain boundary migration (Karato et al., 1986). The density of the hot-pressed sample was measured to be about $3.2\ \text{g/cm}^3$ using the Archimedeian method. We measured infrared (IR) absorption in the wavenumber range of $1500\text{--}4000\ \text{cm}^{-1}$ using an FT-IR spectrophotometer at room temperature. Polished sections of thickness 0.2 mm were used. Hydroxyl species are known to have absorption peaks in the range of $3000\text{--}3700\ \text{cm}^{-1}$ (Paterson, 1982; Chopra and Paterson, 1984). Karato et al. (1986) suggested that the broad absorption peak around $3400\ \text{cm}^{-1}$ is due to free water in inclusions, and the peak in the range of $3400\text{--}3550\ \text{cm}^{-1}$ represents structural hydroxyl species in the solid. We used a relation proposed by Paterson (1982) to calculate the integrated concentration of the hydroxyl species in the wavenumber range from 3200 to $3550\ \text{cm}^{-1}$. The concentration of the hydroxyl species including free water was measured to be about 4000 ppm H/ 10^6 Si in hot-pressed olivine aggregates. Most hot-pressed samples were further cooked in a 1 atm furnace at 1473 K for 3 h with CO–CO₂ gas mixture flow to remove much of the dissolved water. The concentration of the hydroxyl species after cooking is about 300 ppm H/ 10^6 Si. Cooking for longer duration (~ 30 h) did not appear to reduce water content further. No grain growth was found in the cooked samples, but we noticed crack and pore development. The density of the cooked sample is about $3.1\ \text{g/cm}^3$.

Specimens used for shear deformation were prepared by first core-drilling a cooked specimen to get a cylinder of 6.35 mm in diameter and then cutting the cylinder at 45° to its long axis into a number of slices of about 0.5 mm thick. Each slice

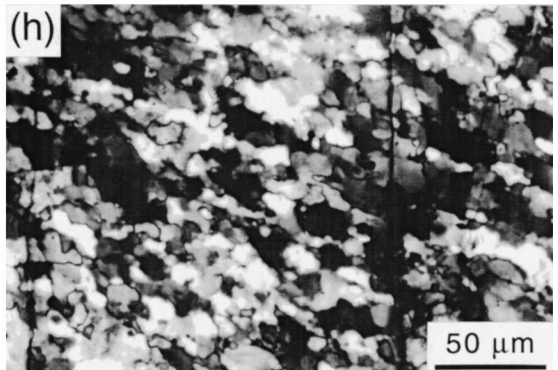
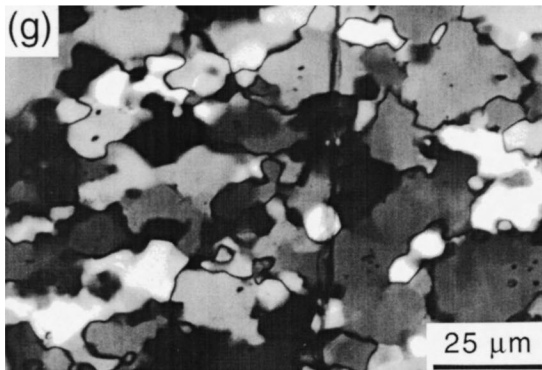
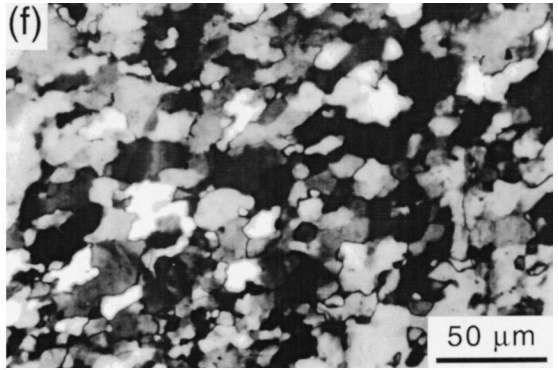
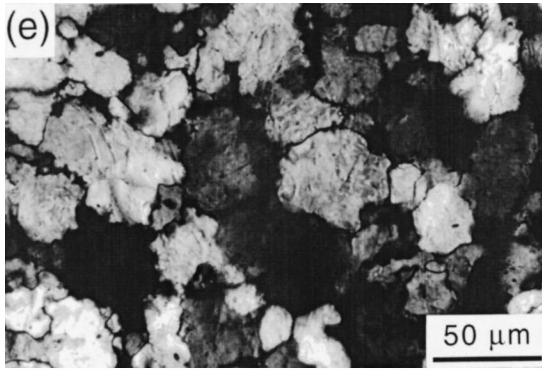
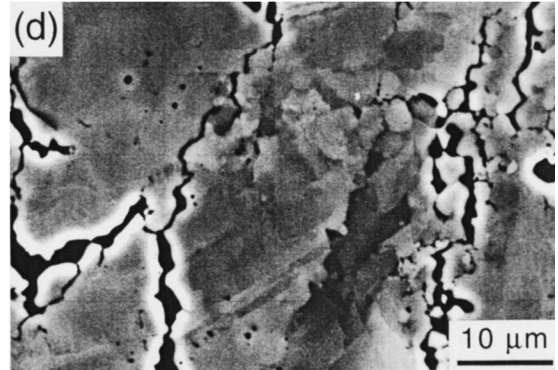
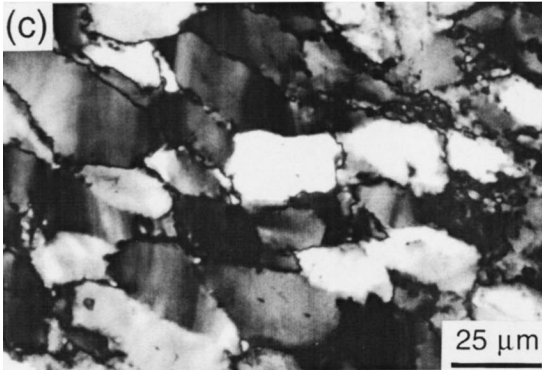
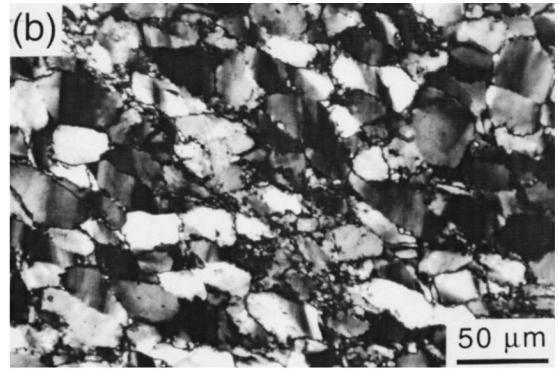
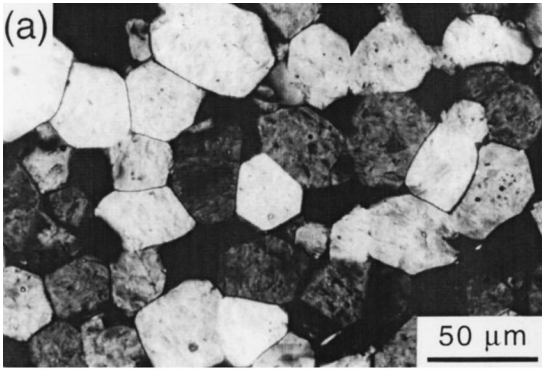


Table 1
Fabrication of olivine aggregates

Specimen	Olivine powder	Hot pressing	Heat treatment	Grain size (μm)	Distribution	Water (ppm H/Si)
SZ-1	<15 μm	1523 K, 300 MPa, water, 6 h	1773 K, 18 h, $f\text{O}_2$ 10^{-6} atm	20–50	bimodal	100
SK-C	50% <5 μm , 50% 5–10 μm	1573 K, 300 MPa, water, 4 h	1673 K, 18 h, $f\text{O}_2$ 10^{-6} atm	32	uniform	150
SZ-2	50% <5 μm , 50% 5–10 μm	1573 K, 300 MPa, water, 8 h	1473 K, 3 h, $f\text{O}_2$ 10^{-6} atm	34	uniform	250
SZ-3	50% <5 μm , 50% 5–10 μm	1573 K, 300 MPa, water, 8 h	–	34	uniform	1000
SZ-4	50% <5 μm , 50% 5–10 μm	1573 K, 300 MPa, water, 8 h	1673 K, 18 h, $f\text{O}_2$ 10^{-6} atm	37	uniform	150

of specimen was then cut into two halves normal to its layer plane (Fig. 2a). The two cut surfaces were coated with platinum of about 20 nm thick. The platinum coating layer evolves into a trail of inclusions along the cutting surfaces during high temperature deformation and thus serves as a passive strain marker that is initially perpendicular to the specimen layer and rotates toward the shear direction with increasing strain (Fig. 2c).

2.2. Specimen assembly for simple shear deformation

A double-shear assembly was used in our early experiments (Fig. 2b). Two layers of specimen were sandwiched between three sliding pistons cut at 45° to their long axes. With this assembly the kinking of the specimen assembly could be minimised and one could ensure a uniform stress and strain distribution within the specimen. However, we found that shear deformation with this assembly tends to localise within one specimen. Because of this, a one-layer shear assembly was utilised in most of our later experiments. The typical speci-

men thickness used in the present study is 0.5 mm. Because of the thin specimen, we could deform the specimen to shear strains of ~ 4 without causing major problems, such as the specimen assembly becoming jammed inside of the internally heated furnace, disruptions to the temperature distribution, etc. (Karato et al., 1998). The specimen and sliding pistons were jacketed into a nickel sleeve (wall thickness of about 1.5 mm). As the flow stress of nickel is lower than 15 MPa at temperatures above 1473 K, part of the lateral movement of the pistons was ‘absorbed’ by the nickel sleeve.

To achieve large shear strains within a thin layer of polycrystalline olivine without sliding along the specimen–slider interfaces and without deformation of the pistons themselves, the sliding pistons have to be at least five to ten times stronger than the olivine and must be non-reactive with olivine. In addition, some regular asperities or grooves are necessary to increase the friction for holding the specimen. We tested a number of piston materials, including alumina (Al_2O_3), fully stabilised zirconia, 2% thoriated tungsten and silicon carbide. We have successfully deformed olivine

Fig. 1. Microstructures. All images except (d) are taken from thin sections under cross-polarised light. (a) Synthetic olivine aggregates, hot-pressed at 1573 K and 300 MPa for ~ 8 h. (b) Specimen PI-284 deformed at 1475 K to a shear strain of 1.1. Shear plane is horizontal and the sense of shear is sinistral. (c) Blow-up of the left bottom corner of (b), showing bands of undulatory extinction within relict grains. (d) Scanning electron microscope (SEM) backscattering image of specimen PI-284; shear plane is vertical and the sense of shear is counter-clockwise. Note nearly equal-dimensioned new grains at rims of large relict grains and sub-boundaries within relict grains revealed by orientation contrasts. (e) Specimen MIT-20 deformed at 1573 K to a shear strain of 0.08, sinistral shear. Note serrated grain boundaries. (f) Specimen MIT-19 deformed at 1573 K to a shear strain of 1.5, dextral shear. (g) Relict grains in MIT-19, subgrains are shown as polygonal-shaped patches of extinction. Transition from subgrains to new grains can be seen from the centre to the rim of many relict grains, suggesting a progressive subgrain rotation mechanism of recrystallisation. Some new grains are also present at migrating (bulging) grain boundaries, indicating a grain boundary migration mechanism of recrystallisation. (h) Specimen MIT-23 deformed at 1573 K to a shear strain of 1.43, sinistral shear. This specimen was saturated with water during deformation.

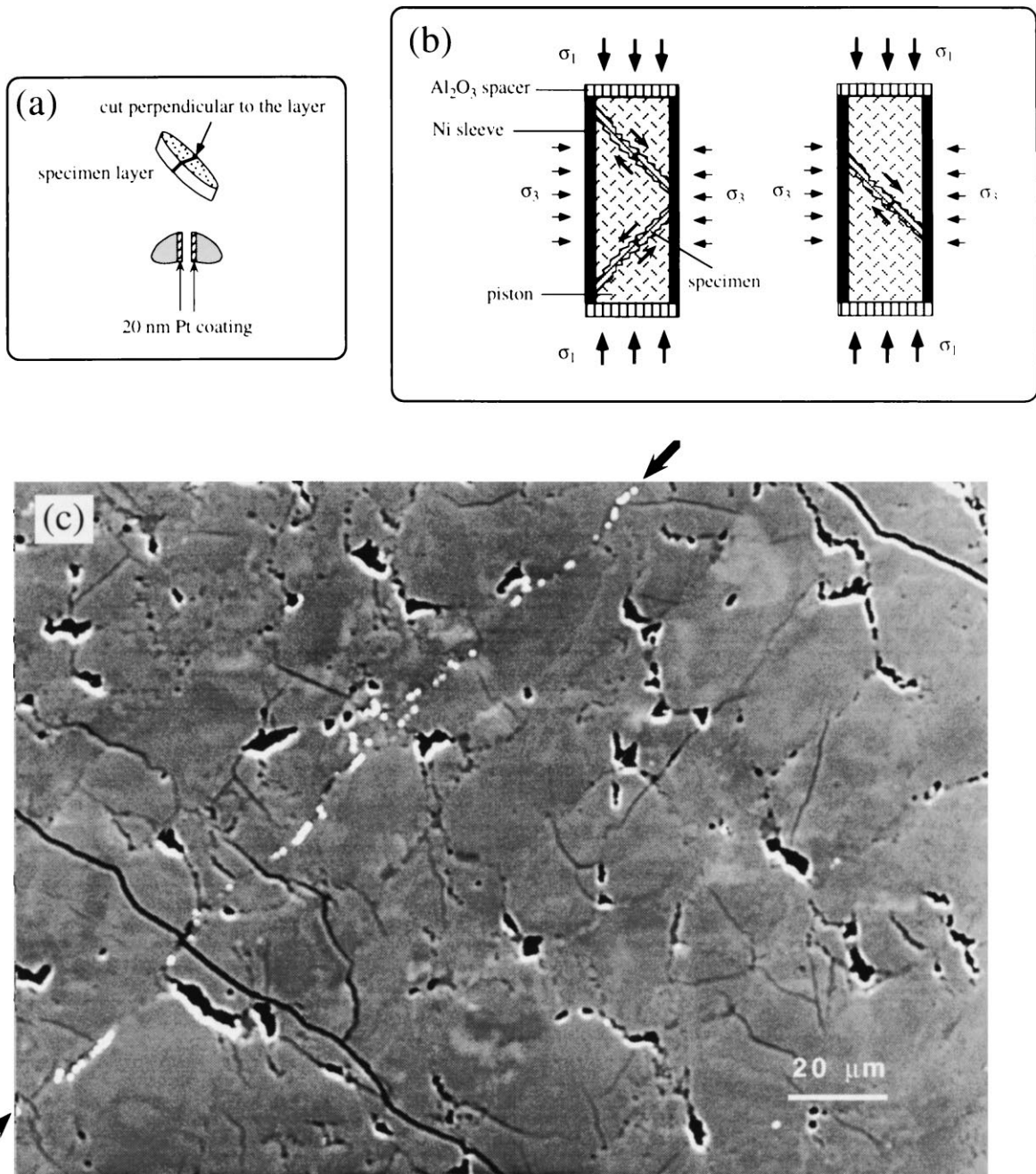


Fig. 2. Specimen assembly for shear deformation. (a) Thin layer of specimen and platinum coating as strain marker. (b) Double-shear (left) and single-layer-shear (right) assembly. (c) SEM micrograph of specimen PI-284 showing the rotated platinum strain marker (the trail of inclusions indicated by the arrows). The platinum marker was horizontal before shear deformation. The shear plane is vertical and the sense of shear is counter-clockwise.

aggregates in simple shear using Al_2O_3 pistons at 1473 K and using 2% thoriated tungsten pistons at 1573 K. The tungsten pistons were grooved with electrical discharge machining wire (0.3 mm diameter) cutting. Grooves of 40 μm depth and 400 μm spacing were produced on the piston surfaces nearly perpendicular to the shear displacement direction. Grooves on the Al_2O_3 piston surfaces were produced using a diamond wire saw.

All our experiments were performed within the stability field of olivine. In the runs with Al_2O_3 as sliding pistons, the $f\text{O}_2$ was likely controlled by the Ni–NiO buffer. In the runs where tungsten pistons were used, the $f\text{O}_2$ was probably controlled by the W– WO_2 buffer.

2.3. Deformation apparatus and experimental procedures

We conducted deformation experiments at temperatures of 1473 K and 1573 K and a nominal axial displacement rate of 4.7×10^{-5} mm/s (nominal shear strain rate about 1×10^{-4} s $^{-1}$). These conditions were chosen so that the synthetic olivine aggregates, of grain size ~ 35 μm , were deformed

well within the dislocation creep regime based on the deformation mechanism map of olivine (Karato et al., 1986).

We used two internally heated, argon-gas-medium deformation apparatus: one is the Paterson Instrument apparatus (hereafter referred to as PI apparatus) and the other an MIT vessel. The PI apparatus provides an excellent temperature profile (within ± 2 K along the specimen) and precise (± 0.1 kN) internal load measurements (Paterson, 1990), but the maximum temperature is practically limited to about 1550 K. Six runs at 1473 K were performed using this apparatus. The relative error in flow stress measurements in our experiments is estimated to be about 2 MPa. The resolution of displacement measurement is about 2.5 μm . One run at 1473 K and eight runs at 1573 K were performed with the MIT vessel (Table 2). The temperature variation along the specimen in the MIT vessel is within ± 5 K. Load in the MIT vessel was measured by an external load cell and, therefore, is confining-pressure-sensitive. By reducing the diameter of a loading piston extension (half inside the vessel, half outside connecting to the load cell), the pressure effect on the

Table 2
A list of shear deformation experiments^a

Run no.	Starting material	Piston material	T (K)	γ	γ_s	ϵ (%)	τ_{max} (MPa)	τ_f (MPa)	$\gamma_s \times 10^{-5}$ (s $^{-1}$)	Remarks
PI-148 ^b	SZ-1	Alumina	1473	0.32	0.17	13	165	165	2.4	sliding
PI-150 ^b	SZ-1	Alumina	1473	0.88	0.30	17	165	135	2.2	sliding
PI-154 ^b	SZ-1	Alumina	1473	2.00	0.45	21	150	115	1.6	sliding
PI-158 ^b	SZ-1	Alumina	1473	2.11	0.65	18	165	115	2.2	sliding
PI-284	SZ-4	Alumina	1473	1.20	1.10	23	239	239	9.6	good
MIT-24	SZ-4	Zirconia	1473	1.50	0.14	9	147	137	0.8	piston def.
PI-496	SZ-4	Alumina	1473	0.80	0.80	–	180	180	9.6	sliding
MIT-5	SK-C	Alumina	1573	2.00	0.11	11	110	95	0.4	sliding
MIT-6	SK-C	Zirconia	1573	2.35	0.65	20	140	150	2.7	piston def.
MIT-17	SZ-2	Tungsten	1573	2.50	1.00	14	100	85	3.3	sliding
MIT-18	SZ-2	Tungsten	1573	1.55	1.15	15	105	65	10	good
MIT-19	SZ-2	Tungsten	1573	1.70	1.50	14	100	75	11	good
MIT-20	SZ-2	Tungsten	1573	0.11	0.08	7	103	103	1.6	good
MIT-21	SZ-2	Tungsten	1573	0.75	0.58	10	95	95	0.7	good
MIT-23	SZ-3	Tungsten	1573	1.77	1.43	13	80	80	9.5	good

^a Note that γ is the shear strain calculated using the applied shear displacement along the sliding surface on the assumption that deformation occurred uniformly across the whole specimen layer. γ and γ_s are the shear strain and the shear strain rate measured using the strain marker. ϵ is the total compression strain. τ_{max} and τ_f are the maximum shear stress reached and the shear stress at the end of the run. See Table 1 for more information about the starting material.

^b Double-shear assembly.

load cell was minimised. Furthermore, during data reduction, the load data throughout each experiment were collected at the same confining pressure. The external load cell has been calibrated with a standard spring, which was put inside of the pressure vessel and was subject to a confining pressure of 300 MPa. A constant displacement rate of 4.7×10^{-5} mm/s, which is the same as in our shear experiments, was used in the calibration to eliminate the effect of time-dependent friction around the loading piston extension. Comparison experiments show that the load measurement with this external load cell is usually less than 5% higher than that measured using the internal capacitor load cell of the PI. The relative error in flow stress measurements with the MIT vessel is estimated to be about 10 MPa.

For all experiments, we first raised the confining pressure to 110 MPa and then increased the temperature at a rate of about 20 K/min. As the temperature reached 1273 K the confining pressure was increased to 300 MPa. After the temperature reached the designated value, annealing for 1 h was performed before shear deformation to eliminate the pores formed during previous depressurisation and cooking at room pressure and to enhance the ‘bonding’ between sliders and specimen. After deformation, the load was first removed and the specimen was then quenched to room temperature and room pressure.

2.4. Microstructural analysis

2.4.1. Thin section preparation

The iron jacket and the nickel sleeve surrounding the deformed specimens were dissolved using 1:1 HCl–HNO₃ solution. The deformed specimen and attached pistons were then cut using a diamond saw along the plane containing the compression axis and maximum shear displacement (*XZ* section of the finite strain ellipsoid, $X \geq Y \geq Z$). Doubly polished thin sections about 10–20 μm thick were prepared.

2.4.2. Universal stage technique

Crystallographic orientations of large ($> 20 \mu\text{m}$) relict grains of olivine were measured using a universal stage. The orientations of two of the

three crystallographic axes, [100], [010], and [001] of olivine were measured directly and that of the third axis was calculated. Measurements of 130–210 grains were usually performed within the central part of the specimen. Pole figures of [100], [010], and [001] were plotted using a Macintosh version of ‘Steroplot’.

2.4.3. The EBSD technique

The lattice orientations of both large relict grains and finely ($< 10 \mu\text{m}$) recrystallised grains in four specimens (Table 1) were measured using the EBSD technique. Specimens were cut along the *XZ* plane. The cut surfaces were first polished with Al₂O₃ powder of 10–0.5 μm in size and finished by 0.05 μm colloidal silica on a vibration polisher. The specimen was then cleaned and coated with a thin layer of carbon. Backscattered electron images showing orientation contrast in the central part of the specimens serve as a grain-scale map. Lattice orientations for individual grains were then measured on a Jeol-6400 SEM with a tungsten filament.

EBSD patterns are formed in an SEM when a stationary incident electron beam produces back-scattered electrons that are Bragg diffracted (Dingley and Randle, 1992; Wright and Adams, 1992). We used a sample tilted 70°, a working distance of 23 mm, an acceleration voltage of 20 kV and a probe current of 1×10^{-8} A. The diffraction pattern was detected using a NORDIF system (a phosphor screen, a low light CCD camera, and a Hamamatsu image processor). The ‘*hkl*’ software system (Channel +) was used to detect bands and to provide solutions of lattice orientations for each EBSD pattern. For each specimen, we selected a few areas from the image map and conducted systematic measurements for all grains within the selected areas. Within most large relict grains, a number of sub-boundaries are present. In such cases, we recorded only one measurement near the grain centre to avoid biasing the measured preferred orientations. For the purpose of analysing active slip systems, we attempted systematic measurements of subgrain orientations inside a number of large relict grains.

3. Results

3.1. Partitioning of compressional strain and shear strain

Measurements of the change in sample thickness and the rotation of the platinum strain marker respectively provide the total compressional strain ϵ and the shear strain γ_s listed in Table 2. The total compressional strain was calculated from the change in specimen thickness associated with both the 1 h annealing before deformation and with the shear deformation. Based on an experiment that was annealed for 1 h but was aborted before the start of shear deformation, we determined the change in specimen thickness during the isostatic annealing to be about 4%. The compressional strain during shear deformation also rotates the platinum strain marker because the marker is initially at 45° to the maximum principal stress direction. Thus, the shear strain γ_s calculated from the rotation of the strain marker is the maximum value. In Fig. 3, we plotted the compressional strain during shear deformation against the shear strain γ_s . The dashed line represents the effect of the compressional strain on the rotation of strain

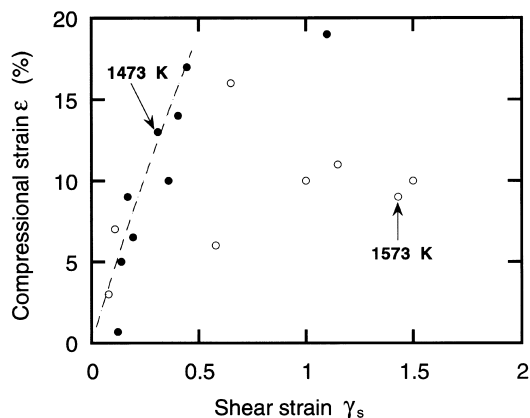


Fig. 3. Partitioning of compression strain and shear strain during shear deformation. The compression strain is the total compression strain listed in Table 2 minus the 4% strain that occurred during the 1 h annealing before shear deformation. Shear strain here is the value measured with the strain marker. Each point in the diagram represents one shear deformation experiment. The dashed line represents the maximum strain marker rotation due to compressional strain.

marker, assuming a constant volume and homogeneous deformation during axial compression. It shows that axial compression is dominant at nominal shear strains <0.5 , whereas at nominal shear strains >1 a predominant shear deformation was achieved.

3.2. Shear strain versus shear stress

Shear strains were measured both from the rotation of the strain marker γ_s and from the axial displacement transducer γ . A significantly lower value of γ_s than γ indicates either sliding along the piston–specimen interfaces or deformation of the sliding pistons themselves (Table 2). Localised sliding along piston–specimen interfaces occurred in experiments PI-148, PI-150, PI-154 and PI-158. It was caused by the formation of reaction zones (a few micrometres thick) between the olivine and the Al_2O_3 pistons. These runs are characterised by strain softening behaviour (Table 2). This interface sliding problem was prevented in our later runs (e.g. PI-284) by increasing the size of the surface asperities on the Al_2O_3 pistons. In the runs MIT-24 and MIT-6, where fully stabilised zirconia was used as sliding pistons, steady state deformation was observed due to the deformation of sliding pistons.

A constant axial displacement rate of 4.7×10^{-5} mm/s was used for all our experiments. However, the actual average shear strain rate varied from about 0.4×10^{-5} s $^{-1}$ in those runs that showed significant piston–specimen interface sliding or piston deformation, to about 10×10^{-5} s $^{-1}$ in the more successful runs (Table 2). With increasing shear displacement, the contact area between the pistons and the olivine specimen decreases, leading to a lower nominal stress. This effect has been corrected in the determination of stress.

Fig. 4 shows the typical shear strain γ –shear stress τ curves for olivine aggregates. It is clear that temperature has a strong effect on the strain–stress behaviour of olivine aggregates. The specimen deformed at 1473 K shows a pronounced strain hardening up to a shear strain of 1.1. In contrast, specimens deformed at 1573 K with a similar amount of structural water (~ 300 ppm H/ 10^6 Si) show a moderate softening after shear

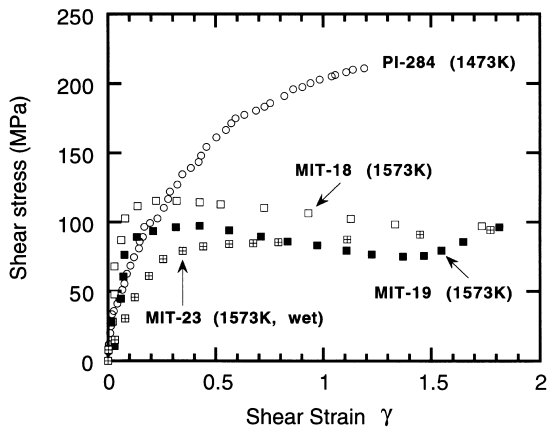


Fig. 4. Shear strain–shear stress curves of olivine aggregates. Note the reasonably good reproducibilities.

strains of ~ 0.6 . One specimen (MIT-23) was deformed at 1573 K with ~ 4000 ppm H/ 10^6 Si water. A comparison with other samples deformed at 1573 K with less water shows that this ‘wet’ sample has a lower yield strength and a slight strain hardening, which is probably due to a gradual loss of water during the experiment.

3.3. General microstructures

The microstructures are very different between samples deformed at 1473 K and at 1573 K. In samples deformed at 1473 K the relict olivine grains are elongated with aspect ratios roughly consistent with the finite strain ellipsoid based on the assumption of simple shear deformation (Fig. 1b and c). For example, at a shear strain of 1.1 most grains have an aspect ratio of 2:1 to 3:1, although ribbon bands with aspect ratios as high as 7:1–8:1 can be observed locally. Bands of undulatory extinction are present in most grains and the band boundaries are commonly aligned at high angles to the shear plane (Fig. 1c). Universal stage measurements suggest that most band boundaries are (100) subgrain boundaries. Dynamically recrystallised new grains were formed along the rims of elongated relict grains in specimens deformed to shear strains >0.7 . Observations using scanning electron microscopy show that most new grains are near equal-dimensional and have an average size of 1–2 μm (Fig. 1d). The degree

of recrystallisation is about 10 vol.% in the specimen deformed to a shear strain of 1.1.

In samples deformed at 1573 K, grain boundaries become serrated after a shear strain of 0.08 (Fig. 1e). In samples sheared to larger strains the elongations of relict grains are much smaller than those predicted by the finite strain ellipsoid (Fig. 1f and g). Most of the large, elongated grains are actually composed of a number of subgrains with misfit angles of less than 7° (Fig. 1g). Dynamically recrystallised new grains make up to almost 20 vol.% in samples deformed to a shear strain of 0.6 and increase to about 50 vol.% at a shear strain of 1.5. The sample deformed to a shear strain of 1.43 and saturated with water (MIT-23) has a large amount of recrystallisation (Fig. 1h). Despite the high degree of dynamic recrystallisation, a foliation is extremely well defined by the alignments of the long axes of the large relict grains and non-equal-dimensional recrystallised grains (Fig. 1f and h). Measured foliation orientations roughly follow the orientation of the finite strain ellipsoid, although they vary from one location to another within about 5 – 8° in the specimen. For example, for specimen MIT-23, deformed to a shear strain of 1.43 (Table 2), the average angle θ between foliation and shear direction should be about 27° ($\tan 2\theta = 2/\gamma_s$). The measured angles ranged from 22 to 29° .

The sizes of recrystallised grains were measured in thin sections and etched polished sections under optical microscopy and from SEM backscattering images. The grain size is calculated as the mean intercept length multiplied by a geometry factor of 1.2 (van der Wal et al., 1993). The number of measurements in each specimen ranges from 30 to about 250 grains. In Fig. 5 the recrystallised grain size D_g is plotted against the axial differential stress ($\sigma = \sigma_1 - \sigma_3$) near the end of the deformation. A grain size–flow stress σ relationship of $D_g = 0.015\sigma^{-1.33}$ is shown as a reference. This relationship was determined by van der Wal et al. (1993) for experimentally deformed Anita Bay and üheim dunite, which contains up to 10 vol.% of silica-rich melt. It is clear that, at the same flow stress, the recrystallised grain sizes in our experiments are systematically lower than those of van der Wal et al. (1993) by a factor of about

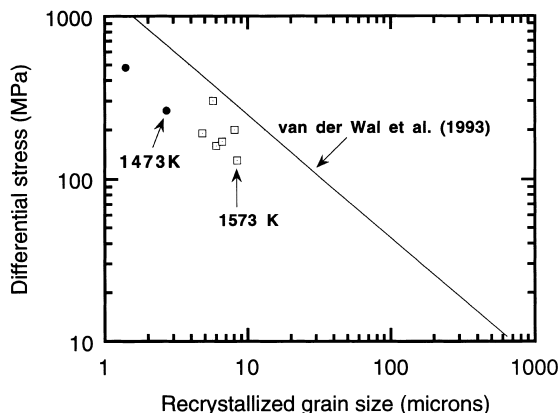


Fig. 5. Relationship between flow stress and recrystallised grain size.

two. However, the $\log(\text{grain size})-\log(\text{stress})$ slopes appear similar for the two studies. The reason for the smaller recrystallised grain sizes in our samples is not well understood.

The distribution of recrystallised grain sizes was examined in three specimens deformed at 1573 K (Fig. 6). Corresponding to a reduction of final shear stress from 95 MPa in specimen MIT-21 to about 65 MPa in specimen MIT-18 (Table 1), the mean grain size increased from ~ 5 to 8 μm , but the grain size distribution remained similar, which is indicative of normal grain growth. Specimen MIT-23 was deformed to a shear strain of 1.43 under ‘wet’ condition (Table 1). The final shear

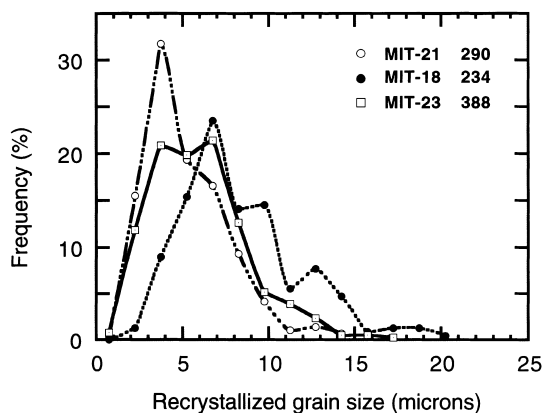


Fig. 6. Distribution of recrystallised grain sizes along lines perpendicular to the shear direction. The number of measurements is shown beside the specimen number.

stress is about 100 MPa and the mean intercept is $\sim 6 \mu\text{m}$. However, there is a wide distribution of intercepts (4 to 7 μm are equally populated), suggesting that grain growth could have been partially restricted.

3.4. LPO

3.4.1. Orientations for relict grains

The lattice orientations of relict grains larger than about 20 μm were measured using mainly the universal stage technique (Figs. 7 and 8). The EBSD technique was used only in three samples (Figs. 9 and 10). Pole figures for specimens deformed at 1473 K are shown in Fig. 7. The dashed line S and the solid line C represent the strain ellipsoid and shear direction respectively. The strain ellipsoid is calculated from the rotation of the strain marker, assuming a predominant simple shear deformation. In specimens deformed up to a shear strain of 1.1 at 1473 K (Fig. 7e), [100] peaks roughly follow the foliation (strain ellipsoid) direction, [010] peaks are normal to or at high angle to the foliation plane, and [001] are parallel to foliation but perpendicular to the foliation direction. We also noted that, in most samples, [100] axes also display a minor peak at the [001] major peak position. The presence of double maxima of [100] and [001] may indicate that two slip directions operated during shear deformation.

In the specimen deformed to a shear strain of 1.1 at 1473 K, measurements using the EBSD technique show that the wide angular range of [100] axes revealed by the universal stage measurements is actually composed of two girdles: a main girdle parallel to the shear plane and a minor girdle perpendicular to the maximum principal (compressive) stress direction σ_1 (Fig. 9a). [010] axes show strong maxima perpendicular to the shear plane. The pole figure for [001] axes is generally weak, with some alignment parallel to the shear direction. The alignment of both [100] and [001] axes parallel to the shear direction suggests the operation of slip systems involving both $b=[100]$ and [001].

At 1573 K (Fig. 8), at shear strains lower than ~ 0.6 , lattice orientations of olivine seem to be related to the strain ellipsoid, but to a lesser extent

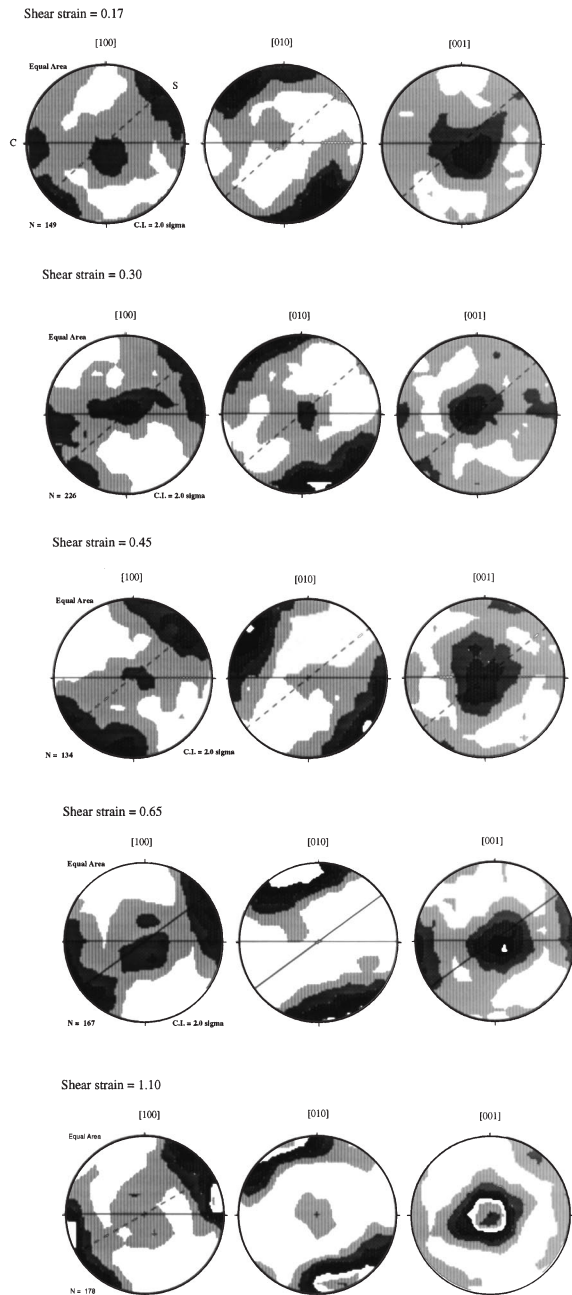


Fig. 7. LPOs of relict olivine grains deformed at 1473 K to different shear strains as indicated; universal stage measurements. Lower hemisphere projection and Kamb contour plot were used. S and C represent finite strain ellipsoid and shear plane respectively. N and C.I. are the number of measurements and contour interval respectively. The sense of shear is dextral for all pole figures.

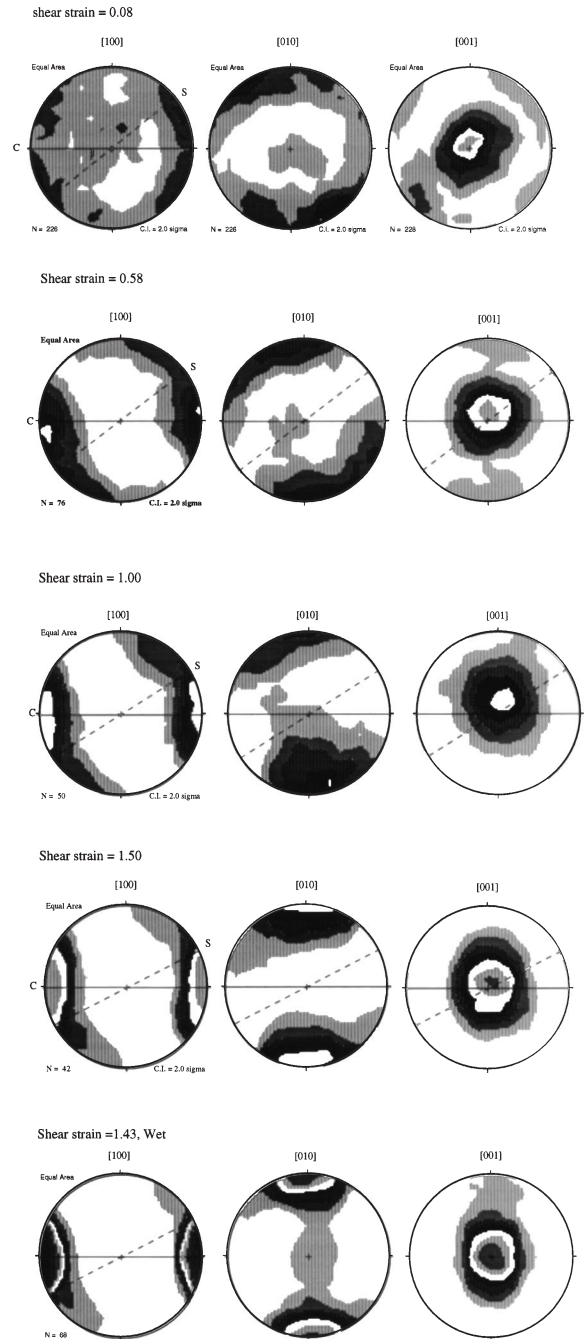


Fig. 8. LPOs of relict olivine aggregates deformed at 1573 K to different shear strain as indicated; universal stage measurements. Again, lower hemisphere projection and Kamb contour plot were used. Dextral shear for all pole figures.

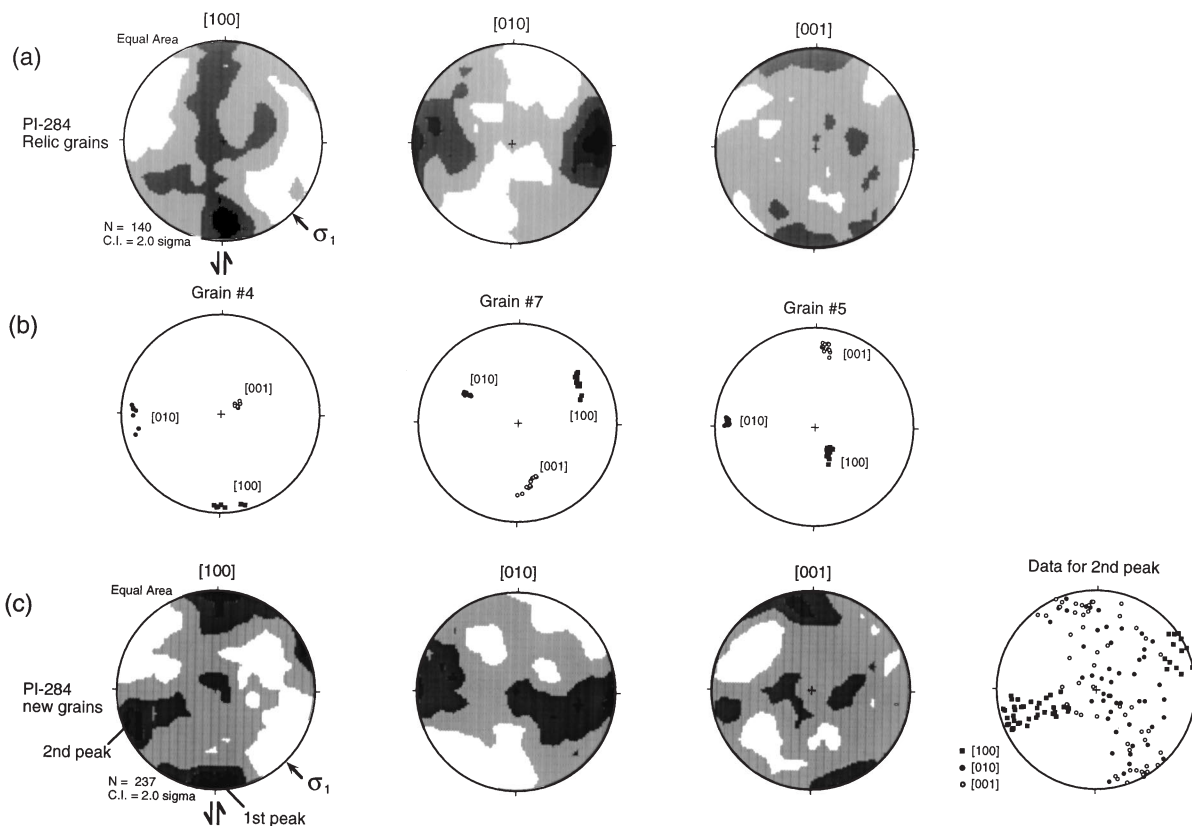


Fig. 9. EBSD measurements of lattice orientations of olivine grains in specimen PI-284 deformed at 1473 K. Stress and shear directions shown apply to all pole figures. (a) Pole figures for large relict grains. (b) Subgrain misorientations within individual relict grains. (c) Pole figures for recrystallised new grains.

than at 1473 K. Those minor peaks observed at 1473 K were not found. With increasing shear strain the lattice orientations rotate toward the shear direction at a rate much faster than the finite strain. At a shear strain ~ 1 , the lattice orientations assume flow-geometry-control, with [100] parallel to the shear direction, [010] normal to the shear plane, and [001] within the shear plane and perpendicular to the shear direction. The peak strength of the lattice orientations increases with increasing shear strain. The sample deformed under 'wet' conditions (MIT-23) shows even stronger (more concentrated) peaks of [100], [010], and [001], which are related to the flow geometry (Fig. 8e).

EBSD measurements were done on two samples deformed at 1573 K (Fig. 10a and d). The LPO pattern is similar to those determined with the universal stage technique.

3.4.2. Orientations for subgrains

Determination of misorientation axis of subgrain boundaries in large relict grains can be used to determine the active slip systems on the assumption that lattice reorientation is controlled by crystal slip (Lloyd and Freeman, 1991, Lloyd and Freeman, 1994). This can be done with the EBSD technique by performing linear scans across a grain and monitoring rotations of a EBSD pattern with similar zone axes.

In specimen PI-284, deformed to a shear strain of 1.1 at 1473 K, we made 101 measurements in total for ten randomly selected relict grains. Fig. 9b shows subgrain rotations within three of these grains. The maximum lattice rotation angle across any relict grains is about 20° . In grain #4 and grain #7 the rotation axis is near [001] and [010] respectively. Because the slip plane normal and

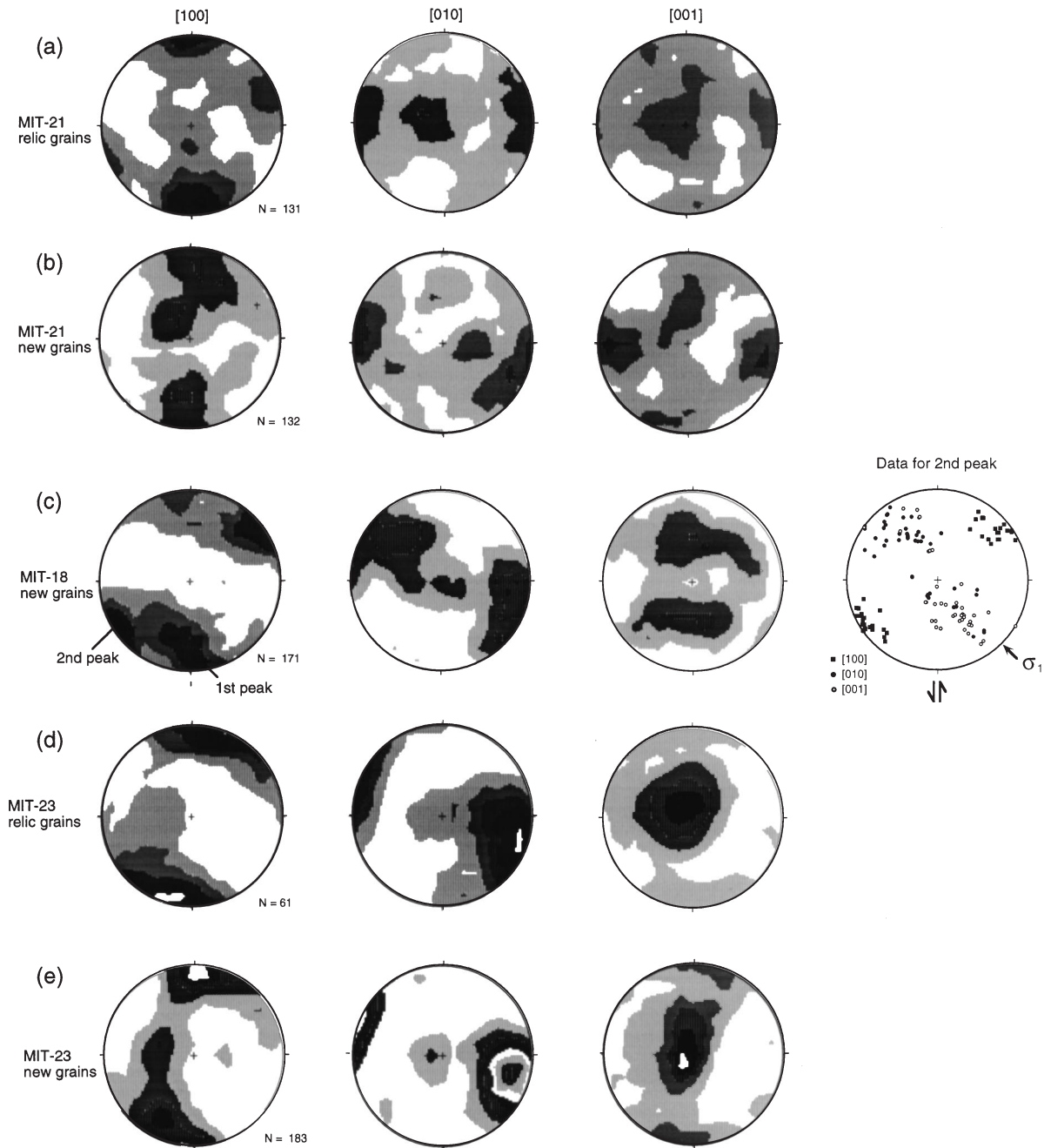


Fig. 10. EBSD measurements of lattice orientations for olivine grains in three specimens deformed at 1573 K. Stress and shear directions shown apply to all pole figures. (a) Pole figures for relict grains in specimen MIT-21. (b) Pole figures for new grains in specimen MIT-21. (c) Pole figures for new grains in specimen MIT-18; note a bimodal pattern of [100] fabric. We did ~30 measurements (not shown here) for the relict grains in MIT-18; the pattern of lattice orientations is similar to (d) for MIT-23. (d) Pole figure for relict grains in specimen MIT-23. (e) Pole figure for recrystallised new grains in specimen MIT-23.

slip direction should be perpendicular to the rotation axis, the possible slip systems are (010)[100] for grain #4 and (100)[001] or mixed [100] and [001] slip directions for grain #7. In the other eight grains, for example grain #5 (Fig. 9b), all three cardinal directions are re-oriented so that no simple rotation axis can be clearly identified.

In specimens deformed at 1573 K the total rotation angle between subgrains within each relict grain is usually $\sim 5\text{--}10^\circ$, which is too small to be useful for determining active slip systems. The small total rotation angle could be due to the fact that grain growth and grain-boundary migration are significantly easier at 1573 K than at 1473 K. We measured subgrain orientations for about 15 relict grains in specimen MIT-21. Only two of them (not reproduced here) clearly show a rotation consistent with slip systems of (010)[100] and (010)[001]. We measured subgrain orientations for 14 relict grains in specimen MIT-23. Only two grains clearly show a rotation consistent with slip systems of (010)[100].

3.4.3. Orientations for recrystallised grains

Recrystallised new grains can be easily distinguished from subgrains by changes of the EBSD pattern which are indicative of misorientations much higher than 5° . For the recrystallised grains in specimen PI-284 the [100] axes show a bimodal maxima pattern (Fig. 9c). One component of the [100] maxima is parallel to the shear direction, and the other at $\sim 60^\circ$ to the shear direction. The bimodal pattern is not obvious in [010] and [001] pole figures: [010] axes form partial girdles roughly perpendicular to the shear plane. [001] fabric is weak, but with some concentrations of [001] axes either parallel or at high angle to the shear direction. For those grains in the [100] pole figure lying $\sim 60^\circ$ to the shear direction, corresponding [010] and [001] axes are distributed along girdles at $\sim 30^\circ$ to the shear plane, but at 15° to σ_1 (see Fig. 9c, data for second peak).

Specimens MIT-21 and MIT-18 were deformed at 1573 K to shear strains of 0.58 and 1.15 respectively (Table 1). In specimen MIT-21 the LPO for the recrystallised grains is similar to that for relict grains, but weaker (Fig. 10a and b). In contrast, the recrystallised grains in specimen MIT-18 show

an LPO distinctly different from their parent grains (Figs. 8c and 10c). The [100] axes for the recrystallised grains clearly show a bimodal maxima pattern. One component of [100] pattern is parallel to the shear direction, and the other lies in a point maximum perpendicular to σ_1 . For grains belonging to the second component of the [100] pattern, [010] and [001] axes are clustered at approximately 45° to σ_1 (Fig. 10c, data for second peak).

Specimen MIT-23 was also deformed at 1573 K, but the starting material was 'wet'. The LPOs for recrystallised grains are shown in Fig. 10e. In contrast to the point maxima pattern for relict grains (Fig. 10d), [100] and [001] axes of recrystallised grains form girdles sub-parallel to the shear plane. A bimodal pattern of [100] axes is not observed.

4. Summary and discussion

Our experimental studies provide a first set of data on the development of lattice orientations and the corresponding mechanical behaviour of olivine aggregates deformed in simple shear to large strains. We found a marked difference in both fabric development and mechanical behaviour between that at 1473 K and that at 1573 K. At 1473 K the LPO evolves following nearly the strain ellipsoid, and significant strain-hardening occurs. In contrast, at 1573 K a significant deviation from strain-control LPO occurs for shear strains > 0.6 , at which significant strain-softening and dynamic recrystallisation occur. The LPO for relict grains at 1473 K is characterised by a double peak of [100] and [001], suggesting the operation of multiple-slip systems, whereas at 1573 K the LPO is characterised by a strong [100] maximum parallel to the flow direction with the (010) plane parallel to the flow plane, indicating the dominance of a single slip system: [100](010). In contrast, the LPO for recrystallised grains shows a rather complicated relationship with flow geometry and stress or strain ellipsoid.

4.1. Comparison with model predictions

In Fig. 11 we plot the angle of the [010] maximum peak with respect to the shear direction

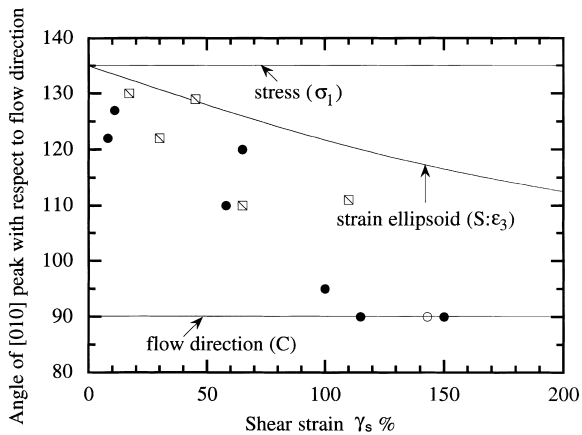


Fig. 11. Comparison of experimental LPO data with model predictions. Filled circles show the data at 1573 K under 'dry' conditions, an open circle shows a data point at 1573 K under water-saturated conditions, and open squares represent the data at 1472 K under 'dry' conditions. The LPO data show a transition from strain-ellipsoid-control at low shear strains to flow-geometry-control at high shear strains.

against shear strain γ_s for the relict grains. The predictions by the three simple models for the development of LPO are also shown. Each point in Fig. 11 represents one experiment. Our experimental data do not agree completely with either of the existing models. At low shear strains our LPO data are roughly consistent with predictions based on polycrystal plasticity theory (Parks and Ahzi, 1990; Takeshita and Wenk, 1990; Ribe and Yu, 1991; Wenk et al., 1991). All the above model predictions are based on the assumption that there are only three independent slip systems, i.e. (010)[100], duplex (001)[100]+(100)[100], and (010)[001], in olivine deformed at high temperatures (Durham and Goetze, 1977; Mackwell et al., 1985; Bai et al., 1991). Therefore, the strain compatibility among grains during deformation of polycrystalline olivine can only be satisfied by either adding artificial slip systems or by relaxing the constraints.

Our LPO data for specimens deformed at 1573 K to large shear strains are consistent with the prediction of the kinematic models. Through a systematic study of massive peridotites and ophiolites, Nicolas and co-workers found an obliquity of LPO of olivine with respect to foliation (Nicolas

et al., 1971; Mercier and Nicolas, 1975; Nicolas, 1976). They argued that the obliquity is an indicator of rotational deformation and can be used to determine the sense of shear. Nicolas et al. (1973) conducted a number of uniaxial compression experiments on a synthetic dunite. Although the LPO fabric in their experiments has an axial symmetry that is similar to those by Avé Lallemant and Carter (1970), by carefully analysing the relationship between the elongation directions of bubbles within the grains and LPO they demonstrated that the LPO of olivine is kinematically controlled. Etchecopar and Vasseur (1987) simulated the LPO development of olivine based on purely geometric considerations. They assumed that a unique slip system (010)[100] operates in all grains of olivine and that the gaps and overlaps produced by heterogeneous deformation were absorbed by dynamic recrystallisation. Their simulation reproduced the flow-geometry-controlled LPO with some success.

4.2. Causes for the transition of LPO from strain control to flow geometry control

Two factors may have contributed to the LPO transition from more or less strain control at low strains to shear geometry control at higher strains in relict olivine grains. One factor is the axial compression strain, which was about 10–15% and occurred mainly at shear strains <0.5 in our experiments. Under uniaxial compression the [010] axes will rotate toward σ_1 , and [100] and [001] form girdles within the plane perpendicular to σ_1 (Avé Lallemant and Carter, 1970; Nicolas et al., 1973). Assuming LPO always follows the shear geometry during a purely simple shear deformation, then the axial compression will tend to rotate [010] away from the shear-plane-normal position and move toward the σ_1 direction. However, we do not think that the axial compression played a major role in our experiments for the following reasons. Firstly, the compression strains in our experiments are too low to result in distinct preferred orientations. As demonstrated by both uniaxial compression experiments (Nicolas et al., 1973; Avé Lallemant and Carter, 1970) and computer modelling (Takeshita and Wenk, 1990; Wenk et al., 1991), no distinct texture pattern can be

formed by axial strain lower than about 30%. Secondly, [100] and [001] axes in our experiments do not display an axial symmetry or an overlapping pattern of axial symmetry with monoclinic symmetry.

A more plausible mechanism for the transition from strain control to shear geometry control is dynamic recrystallisation. As described in the Section 3.3, significant dynamic recrystallisation occurred in our samples deformed at 1573 K to shear strains >0.6 . Dynamic recrystallisation presumably reduced the strain incompatibility between neighbouring grains by recovering the polyhedral shape of grains while preserving their lattice orientations and, therefore, enhanced the deformation by the dominant slip system, (010)[100] (Etchecopar and Vasseur, 1987), to result in a single slip LPO.

4.3. *Effect of fabric development on mechanical behaviour*

The development of shear texture could profoundly affect the mechanical behaviour of rocks. Wenk et al. (1991) modelled plastic deformation of peridotite with the self-consistent theory. They predicted a texture hardening behaviour because crystals progressively rotate into orientations that are less favourably oriented for further slip. Our mechanical results at 1473 K show similarities with the Wenk et al. (1991) model prediction. However, a significant deviation from the theoretical model of Wenk et al. (1991) occurs when dynamic recrystallisation is significant (large strains, particularly at 1573 K). Our observations indicate that the onset of dynamic recrystallisation coincided with the onset of mechanical weakening and the change in LPO toward single slip LPO. Both of these indicate that dynamic recrystallisation relaxes some of the grain-boundary compatibility problems caused by the absence of enough slip systems in olivine. We offer two mechanisms by which dynamic recrystallisation may relax strain compatibility. First, when dynamic recrystallisation occurs a grain-size reduction occurs that promotes grain-size-sensitive deformation mechanisms, such as diffusion creep (Karato et al., 1986). Because the initial conditions in these experiments, as well as

most of deformation conditions in the Earth, are close to the boundary between diffusion and dislocation creep (Karato et al., 1986; Karato and Wu, 1993), the reduction of grain size likely promotes local diffusion creep, thereby relaxing the strain compatibility problem. Second, a change in grain shape caused by recrystallisation could also contribute to relax the strain compatibility problem. In any case, our experimental studies provide strong evidence that dynamic recrystallisation plays a critical role in both LPO developments and in mechanical behaviour.

4.4. *What controls the orientations of recrystallised grains?*

Our EBSD measurements have revealed, under certain conditions, two distinctive patterns of orientations for dynamically recrystallised grains: (a) shear-geometry-controlled orientations with [100] axes parallel to the shear direction; (b) stress-controlled orientations with [100] axes sub-perpendicular to the maximum principal compressive stress. The stress-related orientation pattern was developed where grain boundary migration or growth appears to be significant. We argue below that the shear-geometry-controlled component and the stress-controlled component most likely correspond to subgrain rotation and grain boundary migration processes respectively.

The shear-geometry-controlled orientations were observed for recrystallised grains in all our specimens. Porphyroclasts during shear deformation adopt such shear-geometry-controlled orientations (Figs. 3 and 4), so it is not surprising that new grains formed from relict grains by progressive misorientation of subgrains have similar orientations (Toriumi and Karato, 1985; Karato, 1988).

The stress-controlled orientations are present in specimens PI-284 and MIT-18, but not in MIT-21 or MIT-23. In specimen PI-284, which was deformed at 1473 K, the serrated or lobate grain boundary shapes (Fig. 1a) and recrystallisation at large grain rims suggest that many new grains formed via grain boundary migration (Poirier and Guillopé, 1979; Urai et al., 1986). Specimens MIT-21 and MIT-18 respectively represent an early and a late stage of continuous strain softening

deformation (lower shear stress with increasing shear strain, see Table 1). Following the recrystallised grain size versus stress relationship (e.g. Twiss, 1977; Ross et al., 1980; van der Wal et al., 1993), the mean sizes of recrystallised grains increased with decreasing stress via grain growth. Thus, dynamic grain growth has been more active in the coarser-grained specimen MIT-18 than in MIT-21. Turning to specimen MIT-23, the grain size distribution is broad (Fig. 6), suggesting that the growth of some new grains was inhibited. Because this specimen was saturated with water during high temperature shear deformation, it is likely that water bubbles, or perhaps silicate melt, pinned grain boundaries and retarded grain growth (Karato, 1988; Drury and Urai, 1990). Thus, based on PI-284 and MIT-18, we suggest that grain boundary migration and grain growth appear important for development of stress-controlled lattice orientations. Comparing MIT-21 with MIT-18, dynamic recrystallisation of our olivine aggregates could have been due to subgrain rotation with grain boundary migration recrystallisation at higher strains (Karato et al., 1980, 1982; Lloyd and Freeman, 1994).

The development of stress-controlled lattice orientations for new grains due to grain boundary migration processes was predicted by Karato (1987). Grain boundary migration in deformed aggregates is driven by the differences in dislocation density and elastic strain energy between grains (e.g. Urai et al., 1986). Grain boundaries of grains with low stored strain energy tend to migrate into grains with high energy. Thus, grains with low energy dominate the final preferred orientations. New grains of low-Schmid-factor orientations will have the lowest dislocation densities and dominate the LPOs. Previous studies suggest the active slip systems under our experimental conditions are mainly (010)[100] and (001)[100], so grains with [100] at 90° to the maximum principal stress direction represent the lowest Schmid-factor orientations that would be stable during grain boundary migration (growth). A similar result was obtained for quartz (Gleason et al., 1993).

Stress-controlled LPOs like those reported here are not usually observed in naturally deformed and recrystallised peridotites (Nicolas and

Christensen, 1987). This could be due to the dominant mechanism of dynamic recrystallisation in most natural conditions being subgrain rotation. Some peridotite xenoliths from kimberlite pipes show such LPOs (Mercier, 1985). Recently, Drury and co-workers (personal communication) performed detailed measurements of lattice orientations using the EBSD technique in a natural dunite sample from Oman; they identified two distinctive patterns of lattice orientations that bear striking similarities to those of recrystallised grains in our samples.

When the stress-controlled LPO is present, seismic anisotropy is different from that simply due to flow-geometry-controlled LPO. Calculation of seismic anisotropy from the LPOs of recrystallised grains indicates that the magnitude of P-wave velocity anisotropy is reduced to about 5–7% when stress-controlled and flow-geometry-controlled LPO co-exist, down from 9–10% for LPOs that are controlled only by flow geometry (e.g. in relict grains and MIT-23). Perhaps more importantly, the fast seismic velocity direction becomes oblique to the shear direction and moving towards perpendicular to the maximum principal stress direction. Further studies on naturally deformed samples, as well as more detailed laboratory studies, are essential for geodynamic interpretation of measured seismic anisotropy.

Acknowledgements

We wish to thank David Kohlstedt for allowing us access to many of the facilities of his group. Many thanks are due to Mark Zimmerman and Brad Benson for their assistance in conducting the experiments. We wish to thank Harri Kokkonen for EBSD sample preparation and David Vowles and Frank Brink for their assistance in EBSD measurements. Discussions with Greg Hirth, Peter Hudleston, Christian Teyssier and Basil Tikoff are gratefully acknowledged. This research was supported by NSF grants EAR-9206683, EAR-9220172 and EAR-9706329 to Shun Karato and an ARC postdoctoral fellowship to Shuqing Zhang.

References

- Avé Lallemant, H.G., Carter, N.L., 1970. Syntectonic recrystallization of olivine and modes of flow in the upper mantle. *Geol. Soc. Am. Bull.* 81, 2203–2220.
- Babuska, V., Plomerova, J., Sileny, J., 1993. Models of seismic anisotropy in the deep continental lithosphere. *Phys. Earth Planet. Inter.* 78, 167–191.
- Bai, Q., Mackwell, S.J., Kohlstedt, D.L., 1991. High-temperature creep of olivine single crystals, 1. Mechanical results for buffered samples. *J. Geophys. Res.* 96, 2441–2460.
- Blackman, D.K., Orcott, J.A., Forsyth, D.W., Kendall, J.M., 1993. Seismic anisotropy in the mantle beneath an oceanic spreading centre. *Nature* 366, 675–677.
- Boudier, F., Nicolas, A., 1995. Nature of the Moho transition zone in the Oman ophiolite. *J. Petrol.* 36, 777–796.
- Carter, N.L., Baker, D.W., George, R.P., 1972. Seismic anisotropy, flow, and constitution of the upper mantle. In: Heard, H.C., Borg, I.Y., Carter, N.L., Raleigh, C.B. (Eds.), *Flow and Fracture of Rocks*. Am. Geophys. Union Geophys. Monogr 16, 167–190.
- Chastel, Y.B., Dawson, P.R., Wenk, H.-R., Bennett, K., 1993. Anisotropic convection with implications for the upper mantle. *J. Geophys. Res.* 98, 17757–17771.
- Chopra, P.N., Paterson, M.S., 1984. The role of water in the deformation of dunite. *J. Geophys. Res.* 89, 7861–7876.
- Christensen, N.I., 1984. The magnitude, symmetry and origin of upper mantle anisotropy based on fabric analyses of ultramafic tectonites. *Geophys. J. R. Astron. Soc.* 76, 89–111.
- Dingley, D.J., Randle, V., 1992. Microtexture determination by electron back-scatter diffraction. *J. Mater. Sci.* 27, 4545–4566.
- Drury, M.R., Urai, J.L., 1990. Deformation-related recrystallization processes. *Tectonophysics* 172, 235–253.
- Durham, W.B., Goetze, C., 1977. Plastic flow of oriented single crystals of olivine, 1. Mechanical data. *J. Geophys. Res.* 82, 5131–5753.
- Etchecopar, A., Vasseur, G., 1987. A 3-D kinematic model of fabric development in polycrystalline aggregates: comparisons with experimental and natural examples. *J. Struct. Geol.* 9, 705–717.
- Faul, U.H., Fitz Gerald, J.D., 1999. Grain misorientations in partially molten olivine aggregates: an electron backscatter diffraction study. *Phys. Chem. Miner.* in press.
- Fuchs, K., 1977. Seismic anisotropy of the subcrustal lithosphere as evidence for dynamical processes in the upper mantle. *Geophys. J. R. Astron. Soc.* 49, 167–179.
- Gao, S., Davis, P.M., Liu, H., Slack, P.D., Zorin, Y.A., Mordvinova, V.V., Kozhevnikov, V.M., Meyer, R.P., 1994. Seismic anisotropy and mantle flow beneath the Baikal rift zone. *Nature* 371, 149–151.
- Gleason, G.C., Tullis, J., Heidelbach, F., 1993. The role of dynamic recrystallization in the development of lattice preferred orientation in experimentally deformed quartz aggregates. *J. Struct. Geol.* 15, 1145–1168.
- Hess, H.H., 1964. Seismic anisotropy of the uppermost mantle under oceans. *Nature* 203, 629–631.
- Jessel, M.W., 1988. Simulation of fabric development in recrystallizing aggregates—I. Description of the model. *J. Struct. Geol.* 10, 771–778.
- Ji, S., Zhao, X., Francis, D., 1994. Calibration of shear-wave splitting in the subcontinental upper mantle beneath active orogenic belts using ultramafic xenoliths from the Canadian Cordillera and Alaska. *Tectonophysics* 239, 1–27.
- Ji, S., Rondenay, S., Mareschal, M., Senechal, G., 1996. Obliquity between seismic and electrical anisotropies as a potential indicator of movement sense for ductile shear zones in the upper mantle. *Geology* 24, 1033–1036.
- Karato, S., Wu, P., 1993. Rheology of the upper mantle: a synthesis. *Science* 260, 771–778.
- Karato, S., 1987. Seismic anisotropy due to lattice preferred orientation of minerals: kinematic or dynamic. In: Manghnani, M.H., Syono, Y. (Eds.), *High-Pressure Research in Mineral Physics*. TERRAPUB/AGU, Tokyo/Washington, DC, pp. 455–471.
- Karato, S., 1988. The role of recrystallization in the preferred orientation of olivine. *Phys. Earth Planet. Inter.* 51, 107–122.
- Karato, S., 1989. Grain growth kinetics in olivine aggregates. *Tectonophysics* 168, 255–273.
- Karato, S., Toriumi, M., Fujii, T., 1980. Dynamic recrystallization of olivine during high temperature creep. *Geophys. Res. Lett.* 7, 649–652.
- Karato, S., Toriumi, M., Fujii, T., 1982. Dynamic recrystallization and high-temperature rheology of olivine. In: Akimoto, S., Manghnani, M.H. (Eds.), *High-Pressure Research in Mineral Physics*. Center for Academic Press, Tokyo, pp. 171–189.
- Karato, S., Paterson, M.S., Fitz Gerald, J.D., 1986. Rheology of synthetic olivine aggregates. *J. Geophys. Res.* 91, 8151–8176.
- Karato, S., Zhang, S., Zimmerman, M.E., Daines, M.J., Kohlstedt, D.L., 1998. Experimental studies of shear deformation of mantle materials: towards structural geology in the mantle. *Pure Appl. Geophys.* 151, 589–603.
- Kunze, F., Avé Lallemant, H.G., 1981. Non-coaxial experimental deformation of olivine. *Tectonophysics* 74, T1–T13.
- Levin, V., Park, J., 1998. Quasi-Love phases between Tonga and Hawaii: observations, simulations, and explanations. *J. Geophys. Res.* 103, 24321–24331.
- Lloyd, G.E., Freeman, B., 1991. SEM electron channelling analysis of dynamic recrystallization in a quartz grain. *J. Struct. Geol.* 13, 945–953.
- Lloyd, G.E., Freeman, B., 1994. Dynamic recrystallization of quartz under greenschist conditions. *J. Struct. Geol.* 16, 867–881.
- Mackwell, S.J., Kohlstedt, D.L., Paterson, M.S., 1985. The role of water in the deformation of olivine single crystals. *J. Geophys. Res.* 90, 11319–11333.
- Mainprice, D., Silver, P., 1993. Interpretation of SKS-waves using samples from the subcontinental lithosphere. *Phys. Earth Planet. Inter.* 78, 257–280.

- Mercier, J.C.C., 1985. Olivine and pyroxenes. In: Wenk, H.-R. (Ed.), *Preferred Orientation in Deformed Metals and Rocks: An Introduction to Modern Texture Analysis*. Academic Press, pp. 407–430.
- Mercier, J.C.C., Nicolas, A., 1975. Textures and fabrics of upper mantle peridotites as illustrated by xenoliths from basalts. *J. Petrol.* 16, 454–487.
- Nicolas, A., 1976. Flow in upper-mantle rocks: some geophysical and geodynamic consequences. *Tectonophysics* 32, 93–106.
- Nicolas, A., 1986. Structure and petrology of peridotites: clues to their geodynamic environment. *Rev. Geophys.* 24, 875–895.
- Nicolas, A., Christensen, N., 1987. Formation of anisotropy in upper mantle peridotites — a review. In: Fuchs, K., Froidevaux, C. (Eds.), *Composition, Structure and Dynamics of the Lithosphere–Asthenosphere System*. Am. Geophys. Union Geodyn. Ser. 16, 111–123.
- Nicolas, A., Bouchez, J.L., Boudier, F., Mercier, J.C., 1971. Textures, structures and fabrics due to solid state flow in some European lherzolites. *Tectonophysics* 12, 55–86.
- Nicolas, A., Boudier, F., Boullier, A.M., 1973. Mechanisms of flow in naturally and experimentally deformed peridotites. *Am. J. Sci.* 273, 853–876.
- Parks, D.M., Ahzi, S., 1990. Polycrystalline plastic deformation and texture evolution for crystals with less than five independent slip systems. *J. Mech. Phys. Solids* 38, 701–724.
- Paterson, M.S., 1982. The determination of hydroxyl by infrared absorption in quartz silicate glasses and similar materials. *Bull. Mineral.* 105, 20–29.
- Paterson, M.S., 1990. Rock deformation experimentation. In: Duba, A.G., Durham, W.B., Handin, J.W., Wang, H.F. (Eds.), *The Brittle–Ductile Transition in Rocks*. AGU, Washington, pp. 187–194.
- Peselnick, L., Nicolas, A., Stevenson, P.R., 1974. Velocity anisotropy in a mantle peridotite from the Ivrea zone: application to upper mantle anisotropy. *J. Geophys. Res.* 79, 1175–1235.
- Poirier, J.P., Guillopé, M., 1979. Deformation induced recrystallization of minerals. *Bull. Mineral.* 102, 67–74.
- Ribe, N.M., Yu, Y., 1991. A theory of plastic deformation and textural evolution of olivine polycrystals. *J. Geophys. Res.* 96, 8325–8335.
- Ross, J.V., Avé Lallemant, H.G., Carter, N.L., 1980. Stress dependence of recrystallized grain and subgrain size in olivine. *Tectonophysics* 70, 39–61.
- Takeshita, T., Wenk, H.-R., 1990. Simulation of dislocation-assisted plastic deformation in olivine polycrystals. In: Barber, D.J., Meredith, P.G. (Eds.), *Deformation Processes in Minerals Ceramics and Rocks*. Unwin Hyman, London, pp. 365–377.
- Toriumi, M., Karato, S., 1985. Preferred orientation development of dynamically recrystallized olivine during high temperature creep. *J. Geol.* 93, 407–417.
- Twiss, R.J., 1977. Theory and application of recrystallized grain size paleopiezometry. *Pure Appl. Geophys.* 115, 224–227.
- Urai, J.L., Means, W.D., Lister, G.S., 1986. Dynamic recrystallization of minerals. In: Hobbs, B.E., Heard, H.C. (Eds.), *Mineral and Rock Deformation: Laboratory Studies — The Paterson Volume*. AGU Geophysics Monograph 36, 161–199.
- Van der Wal, D., Chopra, P., Drury, M., Fitz Gerald, J., 1993. Relationships between dynamically recrystallized grain size and deformation conditions in experimentally deformed olivine rocks. *Geophys. Res. Lett.* 20, 1479–1482.
- Wenk, H.R., Christie, J.M., 1991. Comments on the interpretation of deformation textures in rocks. *J. Struct. Geol.* 13, 1091–1110.
- Wenk, H.R., Bennett, K., Canova, G.R., Molinari, A., 1991. Modeling plastic deformation of peridotite with the self-consistent theory. *J. Geophys. Res.* 96, 8337–8349.
- Wenk, H.R., Canova, G., Brechet, Y., Flandin, L., 1997. A deformation-based model for recrystallization of anisotropic materials. *Acta Mater.* 45, 3283–3296.
- Wright, S., Adams, B.L., 1992. Automatic analysis of electron backscatter diffraction patterns. *Metall. Trans. A*: 23, 759–767.
- Zeuch, D.H., Green, H.W., 1984. Experimental deformation of a synthetic dunite at high temperature and pressure: I. Mechanical behaviour, optical microstructure and deformation mechanism. *Tectonophysics* 110, 233–262.
- Zhang, S., Karato, S., 1995. Lattice preferred orientation of olivine deformed in simple shear. *Nature* 375, 774–777.